Soft Matter

PAPER

Cite this: *Soft Matter*, 2023, **19**, 3113

Received 17th January 2023,
Accepted 4th April 2023

DOI: 10.1039/d3sm00065f

rsc.li/soft-matter-journal

High-pressure behavior of hydrophobically coated gold nanoparticle supercrystals: role of the structure

Victor Balédent, Claire Goldmann, Helen Ibrahim and Brigitte Pansu *

We report here an extensive high pressure small-angle X-ray scattering study on 3D supercrystals self-assembled from colloidal spherical gold crystalline nanoparticle (NPs). We used a large variety of NPs with different gold core diameter, from 2 to 10 nm, grafted with different ligands: alkane-thiols or oleylamine. The self assembly of these various NPs leads to supercrystals of different structures: face centered cubic (FCC), body centered cubic (BCC), as well as the C14 Frank and Kasper phase. Using a Diamond Anvil Cell to apply pressure on these wide range of samples, we provide a unique overview on the mechanical properties of gold NPs supercrystals. In particular, bulk modulii have been determined from low pressure regime and the different behavior between FCC and BCC structures has been interpreted as due to an easier restructuring of the ligand conformation in the FCC structure compared to the BCC structure. At higher pressure, a fingerprint of irreversible structural transition has been observed. We have ascribed this irreversibility to the sintering of nanoparticles and confirmed this interpretation by transmission electron microscopy.

1. Introduction

Nanocrystals, used as building blocks, may self-assemble in long-range ordered assemblies, so-called supercrystals (SCs). They are a good example of a *meta*-material as their structural architectures induce collective properties. Thanks to their plasmonic properties in the visible range of the light spectrum, gold supercrystals are notably attractive candidates for optical applications.[1,2] The SCs collective properties depend on both the structure and the distance between the particles within the supercrystals, motivating numerous structural studies by X-ray diffraction.[3] Different structures, namely face-centered cubic (FCC), body-centered cubic (BCC) and Frank–Kasper (C14) phases have been observed,[4] as well as hexagonal compact structures (HCP)[5] for larger particles. The cohesion of these supercrystals is ensured by the van der Waals attraction between the gold cores, in addition to subtle soft shell interactions.[6–9] For this reason, the study of mechanical properties of the ligand shell within SCs is of outmost importance. The supercrystal elastic properties are usually determined from nano-indentation measurements performed with an atomic force microscope on films or on bulk domains.[10–14] Another way to apply stress is to use diamond-anvil cell (DAC), a standard device for applying hydrostatic pressure up to several GPa, used either for hard material or soft matter.[15] This is the setup used in the experimental study of this paper. The ordered structures can be probed by *in situ* small angle X-ray scattering (SAXS). Due to the thickness of the diamond anvils, high intensity X-ray beam with short wavelength is required to overcome the strong absorption of high pressure cells, conditions that are met in synchrotron facilities.[16] Such experiments have been mainly performed on ordered films of spherical gold NPs organized in an FCC phase.[17,18] They showed that gradual elevation of the external pressure from ambient up to 8.9 GPa caused reversible shrinkage of the dimensions of the lattice unit cell. As a result, fine tuning of the interparticle spacing could be achieved. Above 8.9 and up to 13 GPa, the NPs coalesce to form 1D nanostructures (nanorods or nanowires) that order in a hexagonal structure (*P*6*mm* space group). Similar behavior has been reported for other types of particles.[19–21]

In a previous paper,[22] we reported the mechanical behavior of a FCC supercrystal under hydrostatic pressure. Up to 12 GPa, the SC showed a remarkable high structural stability. The bulk elastic modulus of the SC was extracted from SAXS measurements, with a two-step compression: a collapse of the voids between the NPs followed by the compression of the soft matrix which gives a major contribution to the mechanical behavior. In this paper, we report an exhaustive study of pressure induced behavior for different supercrystal structures, various gold core diameters (from 2 to 10 nm) and gold volume fraction, covering a wide pressure range from ambient up to 40 GPa. The main result is that both low and high pressure behavior depends mainly on the structure. The elastic modulus of the ligand

---

Université Paris-Saclay, CNRS, Laboratoire de Physique des Solides, UMR-8502, 91405, Orsay, France. E-mail: brigitte.pansu@universite-paris-saclay.fr; Tel: +33 1 69 15 53 32

matrix measured at low pressure is larger in the BCC structure than in the FCC structure. We associate this behavior to the shape of the volume per NP available for the ligand matrix, different for both structures. At higher pressure, the BCC structure happens to be less stable than the FCC one: an irreversible transition is observed at lower pressure. This difference can be explained by the largest inhomogeneity of the ligand shell in the FCC structure compared to the BCC one. As a consequence, the restructuring of the ligand conformation is therefore more easily achieved in the FCC structure. The mechanical properties of FCC SCs built with different gold core diameters and ligands are also compared and discussed, one sample exhibiting a remarkable structural stability up to 43 GPa.

2 Materials and methods

Different nanoparticles (NPs) have been used in this study. Their characteristics have been listed in Table 1, and are labelled using their structure, core size and ligand type, meaning FCC-5-C12 corresponds to a 5 nm gold core diameter grafted with C12-thiol ligands and self-assembled in FCC structure. Different synthesis routes are required to get stable nanoparticles with gold cores ranging from 2 to 10 nm. The smallest particles (BCC-2-C12 and C14-2-C14) were synthesized by the Brust method in the presence of the final thiol.[23] At the end of the reaction, the solvent was evaporated, the particles were precipitated with ethanol, filtered, washed and stored as a powder. For slightly bigger particles (C14-3-C6, FCC-5-C12, BCC-3-C12, C14-4-C12 and FCC-3-C16), we used a method developed in the lab, using 2 nm particles as seeds. They were regrown using AuCl(PPh3) as a gold precursor. They were washed and stored the same way as 2 nm particles.[24] The biggest particles (FCC-7-Ol, FCC-9-Ol) were prepared in aqueous medium with surfactant, using the multi-step protocol.[25] Once the desired size was reached, the particles were transferred into toluene using oleylamine.[26] The organic phase was precipitated with ethanol and centrifuged. The particles were redispersed in toluene. Organic solvents and the other chemicals were purchased from Sigma-Aldrich Co. and were used as received. The core diameter D_c has been measured by TEM and SAXS using NPs dilute suspensions in toluene. TEM was performed at IMAGIF (I2BC CNRS, Gif s/Yvette, France) using a JEOL JEM-1400 microscope operating at 120 kV with a filament current of about 55 μA. Among other details, TEM pictures of the NPs used in the present article can be found in ref. 24 for NPs between 2 and 5 nm, and in Fig. 8a for the largest ones. SAXS has been performed on the D2AM beamline at ESRF or on the Swing beamline at Soleil. The thiol grafting density ($\approx 5\ \text{nm}^{-2}$) has been determined by thermogravimetric analysis using the 6000@PerkinElmer STA (Simultaneous Thermal Analyzer) at ICMMO (Université Paris-Saclay, France) for at least three batches. This value is coherent with literature[27] and does not depend significantly on the core size. This value is also close to the grafting density expected in the case of oleylamine as ligand.[28]

Table 1 List of the samples used in the experiments, labelled with structure-core size-ligand convention, and their main characteristics: core diameter, polydispersity, ligand, structure. The last column indicate if the sample has been used for low (LP) or high pressure (HP) experiment

Name	D_c (nm)	Disp. (%)	Ligand	Structure	Exp.
BCC-2-C12	2.17	12	C12-thiol	BCC	LP
C14-3-C6	2.71	17	C6-thiol	C14	LP
FCC-5-C12	4.82	9	C12-thiol	FCC	LP,HP
C14-2-C14	2.0	10	C14-thiol	C14	HP
BCC-3-C12	3.2	10	C12-thiol	BCC	HP
C14-4-C12	3.7	13	C12-thiol	C14	HP
FCC-3-C16	3.0	10	C16-thiol	FCC	HP
FCC-7-Ol	7.0	8	Oleylamine	FCC	HP
FCC-9-Ol	9.6	9	Oleylamine	FCC	HP

To perform a controlled self-assembly process, the NPs are dispersed in a volatile oil like toluene or cyclohexane at an intermediate weight fraction (typically 15 wt%). The suspensions are then stirred and sonicated before being poured in cylindrical X-ray glass capillaries (diameter 1.5 mm, WJM glas@) sealed at one end. The full height of the capillaries is typically 10 cm, they are initially half-filled and kept vertically to allow slow evaporation of the solvent by the top at room temperature. After several days, supercrystals appear at the bottom of the capillaries and their structure is monitored by SAXS. When all the solvent is evaporated, the glass capillary is shattered and supercrystals can be extracted. Quick evaporation was performed by pouring a drop of suspension on a PTFE plate coated by a film of 3M Fluorinert Electronic Liquid FC-40. After controlling their structure by SAXS, the supercrystals can easily be retreaved using a metallic tip. After self-assembly either in a glass capillary or on a Teflon plate, several domains (smaller than few tenths of microns) are deposited into a diamond anvil cell with a pressure transmitting fluid medium.

Two transmitting media have been used: silicone oil in the first series of experiments up to 10 GPa and a methanol–ethanol (4 : 1 proportion) mixture up to 40 GPa in a second series. The gyration radius of the Si oil being between 2 and 3 nm[29] is too large to let the oil penetrate inside the supercrystals. Short alcohols are bad solvants for the NPs and are not suspected as well to penetrate inside the supercrystals. All samples have been characterized by SAXS after self-assembly. Comparisons with zero pressure spectra (in DAC with transmitting medium) show no difference of lattice parameters within error bars, confirming the absence of effect of both transmitting media. To apply the pressure, membrane driven diamond anvil cells (DAC) were used. Up to 10 GPa, we used diamonds with 600 μm culets with a CuBe gasket drilled with a 300 micron-diameter hole. Up to 40 GPa, we took 300 μm culets diamonds with stainless steel gasket, limiting the hole to 150 μm in diameter. Some pieces of supercrystal was then placed in the hole, together with a ruby chip and the transmitting medium. The standard ruby fluorescence technique[30] was used to monitor the pressure inside the sample chamber in the DAC. The ruby inside the DAC chamber was excited using a class 3b laser (λ = 405 nm). The fluorescence signal was transmitted to the spectrometer (HR4000 ocean optics; 0.47 nm resolution) *via* an optical fiber that was fixed and not touched during the whole experiment, ensuring the same entrance condition of light on the spectrometer. The whole setup was inside the experimental hutch of Swing beamline where the temperature is monitored and stable.

The ruby fluorescence was first measured before applying pressure, ensuring the calibration of the initial wavelength at vanishing pressure for each ruby chip. The pressure was increased by finite steps, with real-time monitoring of the fit-determined pressure, with some delay to allow the pressure to stabilize. Pressure was measured before and after each SAXS measurement, with variation (typically 0.05 GPa at low pressure) well below estimated and reported uncertainty. The silicone oil is known to remain quasi-hydrostatic up to 10 GPa at room temperature. But at higher pressure, non hydrostaticity is expected.

The supercrystal structure under pressure has been determined by SAXS. All results have been obtained during the Run 20201484 (low pressure) and the Run 20211405 (high pressure) on the Swing beamline of the synchrotron Soleil (France). The energy of the X-ray beam was 16 keV, corresponding to a wavelength of 0.775 Å. The sample-detector distance was D = 0.519 m and the size of the focused beam was typically 0.4 mm(H) × 0.1 mm(V). The wave vector norm q is defined by $q = 4\pi\sin\theta/\lambda$ where 2θ is the angle between the scattered beam and the direct beam. The pixel detector (Eiger 4M, Dectris) is an assembly of several modules, with some gaps between them. The SAXS images obtained show textured ring due to the presence of several domains in the sample insid the DAC. The analysis is thus based on the radially integrated intensity $I(q)$ as a function of the wave vector q for different pressure.

Upon pressure, the lattice parameters will decrease, and as long as the structure remains the same (an approximation valid at low pressure), we can follow them as function of pressure. We can then deduce the total volume per NPs labelled V: $V = a^3/4$ for FCC, $V = a^3/2$ for BCC, $V = \sqrt{2}a^3/12$ for C14 assuming $c = \sqrt{\frac{8}{3}}a$. Independantly, we can determine the gold core volume as function of pressure $V_c(P)$, using the standard gold equation of state $V_c(P) = V_c(0)(1 - P/(B_{\mathrm{Gold}} + B'_{\mathrm{Gold}}P))$, with bulk modulus B_{gold} = 167 GPa and $B'_{\mathrm{Gold}} = 5.72$ as obtained for bulk gold and NPs.[31,32] Thus the matrix volume, defined as the volume occupied by both the void and grafted ligands per NP ($V_M = V_{\mathrm{ligands}} + V_{\mathrm{void}}$) can be extracted using the relation: $V_M = V - V_c$. This is the method used in a previous paper[22] on FCC supercrystal (FCC-5-C12 from Table 1). The volume per particle V as well as the matrix volume per particle V_M extracted for each pressure were fitted the equation of state using the eqn (1) with three parameters V^*, V_0, P^*, from ref. 33.

$$V - V^* = \frac{V_0 - V^*}{1 + \frac{P}{P^*}}. \tag{1}$$

The bulk modulus at vanishing pressure writes then:

$$B_0 = P^* \frac{V_0}{V_0 - V^*}. \tag{2}$$

3. Results and discussion

Two sets of experiments are reported in this paper. First a low pressure series, below 10 GPa, aimed at comparing mechanical behavior such as bulk modlulus of different structure of supercrystals: FCC, BCC and C14. This complete our study previously published[22] on FCC structure in a pressure range where no structural transition is expected. The second series of experiments went up to 45 GPa, to extend our study to eventual structural transition or coalescence as reported in other NPs.[19–21]

3.1 Low pressure behavior

Diffractogramms of the three different structures (FCC-5-C12, BCC-2-C12 and C14-3-C6) are presented in Fig. 1 as function of pressure. As can be seen, we stay in the regime where the structure is not changed as the spectra shape remains the same, with only a slight shift toward large q due distance shrinking under pressure. We extracted the lattice parameters and thus both the volume per particle V and the matrix volume V_M per particle as detailed in the method section. The pressure evolution of the ration V/V_0, V_0 being the volume per particle at ambient pressure is represented in Fig. 2. The evolution of this ratio is quite similar for all the structures. The pressure evolution of the ratio V_M/V_M^0 is represented in Fig. 3, V_M^0 being the matrix volume at ambient pressure. We can see that this ratio decreases quicker for FCC than BCC, indicating that the bulk modulus of BCC structure $B^0_{\mathrm{matrix}}(\mathrm{BCC})$ is larger than the one of FCC structure $B^0_{\mathrm{matrix}}(\mathrm{FCC})$. The same reasoning can be made with C14 structure, resulting in the hierarchy of bulk modulii: $B^0_{\mathrm{matrix}}(\mathrm{BCC}) > B^0_{\mathrm{matrix}}(\mathrm{FCC}) > B^0_{\mathrm{matrix}}(\mathrm{C14})$. The fit using the Rault's model gives for the supercrystal: $B^0_{\mathrm{SC}}(\mathrm{BCC})$ = 8.5 ± 1 GPa, $B^0_{\mathrm{SC}}(\mathrm{FCC})$ = 5.3 ± 1 (as reported in our previous experiment[22]), $B^0_{\mathrm{SC}}(\mathrm{C14})$ = 3 ± 1 GPa. and for the matrix: $B^0_{\mathrm{matrix}}(\mathrm{BCC})$ = 7 ± 1 GPa, $B^0_{\mathrm{matrix}}(\mathrm{FCC})$ = 4 ± 1 Gpa, $B^0_{\mathrm{matrix}}(\mathrm{C14})$ = 1.5 ± 1 GPa. Since the bulk modulus of gold is much larger than the matrix bulk modulus at zero pressure, the bulk modulii B^0_{matrix} and B^0_{SC} are thus simply related through the gold volume fraction ϕ by: $B^0_{\mathrm{matrix}} = (1 - \phi)B^0_{\mathrm{SC}}$. The BCC phase appears for lower gold volume fraction $\phi_{\mathrm{BCC\text{-}2\text{-}C12}}$ = 12% compared to $\phi_{\mathrm{FCC\text{-}5\text{-}C12}}$ = 26% or $\phi_{C14\text{-}3\text{-}C6}$ = 25%.

For classical atoms, or any spherical objects that can be modelized by hard spheres, one could expect that close-packed

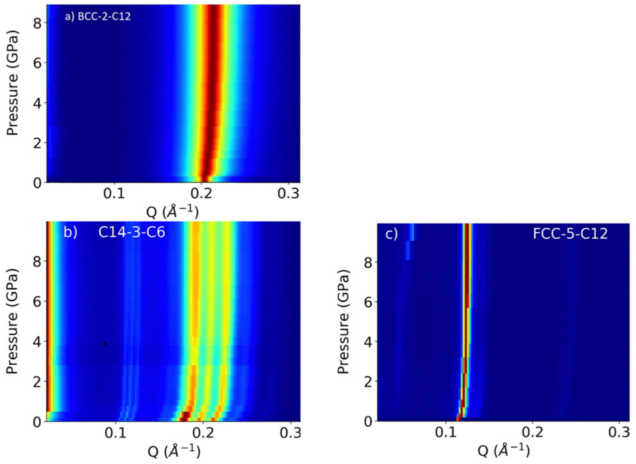

Fig. 1 Color map of the scattering intensity (integrated intensity in log scale) as function of q and pressure in the low pressure regime (below 10 GPa) for samples listed in Table 1 with LP in the last column.

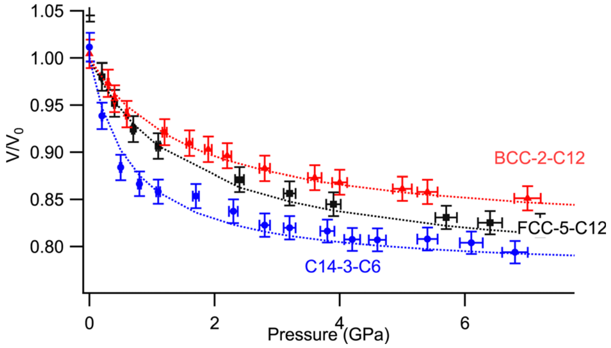

Fig. 2 Variation of the ratio V/V_0 upon pressure for the different structures, where V is the volume per particle and V_0 its limit at vanishing pressure. Lines correspond to the fit using Rault model defined in the text.

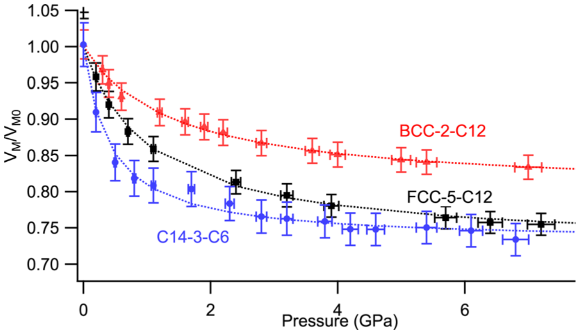

Fig. 3 Variation of the ratio V_M/V_M^0 upon pressure for the different structures where V_M is the matrix volume per particle and V_M^0 its limit at vanishing pressure. Lines correspond to the fit using Rault model defined in the text.

structures with maximum density such as the FCC structure should be less compressible. This is not what we observe in Fig. 2 for soft nanoparticles. An approach beyond the simple hard sphere model is thus necessary. In soft matter, many studies have been performed in diblock copolymer melts[34] that build cubic structures, but some of them are bicontinuous and thus comparison with NP supercrystals is not direct.

This result is part of the general questions raised about compact structure evolution under pressure. Indeed in recent study, the cuboidal BCC to FCC transformation of Lennard-Jones phases under high pressure has been derived from exact lattice Summations in the Lennard-Jones model.[35] However this model is not suited to analyse the structure of the supercrystals built by gold nanoparticles, because of the different nature of interactions between atoms in a crystal (covalent or ionic) and interactions between NPs. In our case, the structure is a consequence of different contribution among which van der Waals attraction between the cores and the combination of attraction and repulsion between the ligands. The Hamaker constant related to the van der Waals attraction between the gold cores through an oil medium is estimated to 75 kT,[36] a relatively high value. The experimental investigation of the ligand distribution in the matrix is not easy. One can first assume that the deviation of the core shape from a perfect spheres due to the faceting of the core is not a dominant parameter since the ligand length largely compensates the deviation from a perfect spherical core. In the following, the core will be thus considered to be perfectly spherical. Neglecting faceting, we advance simple geometrical arguments based on Voronoi tessalation, as in granular materials,[37] in order to explain why FCC and BCC soft structures could behave in a different way under pressure. Around each core, on can draw the volume of all the points that are closer to this core compared to other cores: this is called the Voronoi cell, equivalent to the Wigner Seitz cell for compact structures such as FCC and BCC. It defines the environment of each core and thus the shape of the volume available for the matrix around the core. Such volumes are represented for FCC and BCC structures in Fig. 4.

As can be seen, the BCC Voronoi cell appears more ''spherical'' than the FCC one. The usual way to quantify sphericity of the Voronoi cell, used to understand the phase diagrams of diblock copolymers,[38,39] is the isoperimetric coefficient $\mathrm{IQ} = \dfrac{36\pi V^2}{A^3}$ where V is the cell volume and A its surface area. This ratio is 1 for a perfect sphere, 0.7534 for BCC, 0.7405 for FCC, 0.7613 for C14. As we are mainly concerned by the shell shape, we can introduce other ratios by defining different radii (Fig. 5): the mean radius R_m, the radius of a perfect sphere with the same volume as the Voronoi cell, the external radius R_ext, the radius of the smallest sphere that contains the Voronoi cell, and the internal radius R_int, the radius of the largest sphere contained inside the Voronoi cell. Another way to quantify the deviation to sphericity of the Voronoi cell is the following parameter $\Delta_\mathrm{Voronoi} = \dfrac{R_\mathrm{ext} - R_\mathrm{int}}{R_\mathrm{m}}$: 0.37 for the FCC structure, 0.26 for the BCC one, it vanishes for a perfect sphere. When considering the shell only, its deviation from a spherical shape, assuming a spherical core, Δ_Shell can be written:

$$\Delta_\mathrm{Shell} = \frac{R_\mathrm{ext} - R_\mathrm{int}}{R_\mathrm{m} - R_\mathrm{core}} \tag{3}$$

where $R_\mathrm{m} - R_\mathrm{core}$ is the mean ligand shell thickness around each particle built mainly by the ligands grafted to the gold core but possibly also by interdigitated ligands grafted to the neighbouring particles. Δ_Shell vanishes for a perfect spherical shell but now depends non only of the structure but also on the sample since the BCC structure is observed for larger values of

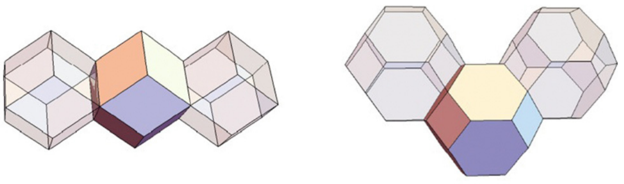
a) b)

Fig. 4 Voronoi cell around each particle: (a) in the FCC structure, (b) in the BCC structure.

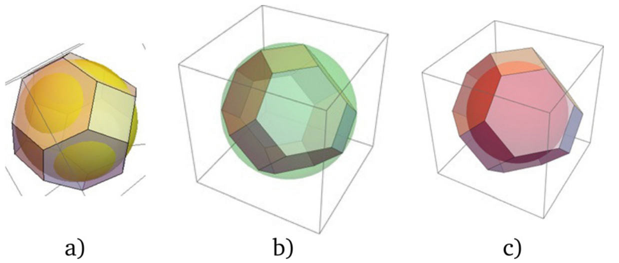

a) b) c)

Fig. 5 Deviation of the Voronoi cell of the BCC structure from a perfect sphere: (a) sphere with the same volume as the Voronoi cell (R_m), (b) smallest sphere that contains the whole Voronoi cell (R_{ext}) (c) largest sphere contained in the Voronoi cell (R_{int}).

$\frac{R_{ext} - R_{int}}{R_m}$. The values for the different supercrystals used in this study at low pressure are collected in Table 2. The conclusion is that, as observed qualitatively, the matrix in the BCC supercrystal is more spherical than in the FCC. The thickness available for ligand is thus more isotropic, meaning a more homogeneous distribution of ligands in the BCC phase. The largest thickness of the matrix in the Voronoi cell $R_{ext} - R_{core}$ can be compared to the ligand extended length L. If the ratio is larger than one, the ligands are not long enough to fill the cell in some directions and this is the case in the FCC cell. Therefore the matrix in the FCC structure contains less dense regions in average or even voids and the ligand distribution in the matrix is less homogeneous. The consequence of such large distribution of ligand density is that they can more easily reorganize under pressure. This can explain why the bulk modulus of the matrix with the same ligands is larger for a BCC structure and why the FCC structure is more stable under high pressure as the void and ligands absorb the deformation. In the C14 structure, there are three different sites and thus one can define only a mean value for Δ_{Shell} =0.78 but it varies between 0.45 and 0.95. As in the FCC structure, the ligands can rearrange under pressure and the matrix bulk modulus is lower than in the BCC phase. This argument is coherent with the previous observation of a larger bulk modulus of the matrix compared to free ligands, measured on FCC-3-C12 sample and pure dodecane samples.[22] This effect was attributed to a less optimized chain packing under pressure compared to the free chains, as the chains are constrained by both grafting and confinement within the soft matrix. This model is based on perfectly spherical cores and this is not the case.[5] Moreover it is important to notice that the curvature of the grafted surface is different for the three samples as well as the number of ligands per particle and the gold volume fraction.

Table 2 List of different radii R_m, R_{int} and R_{ext} as defined in the text, lattice parameter a, the deviation of the Voronoi cell from sphericity Δ_{Shell} and the ratio of the maximum thickness of the ligand shell $R_{ext} - R_{core}$ to the ligand extended length L for the two supercrystals FCC and BCC

	R_m/a	R_{ext}/a	R_{int}/a	a	R_{core}	Δ_{Shell}	$\frac{R_{ext} - R_{core}}{L}$
FCC	$\left(\frac{3}{16\pi}\right)^1/3$	1/2	$\sqrt{2}/4$	9.4	2.4	1.1	1.4
BCC	$\left(\frac{3}{8\pi}\right)^1/3$	$\sqrt{5}/4$	$\sqrt{3}/4$	4.45	1.08	0.5	0.9

3.2 High pressure study: irreversible structural transition

The second series of experiments were performed at higher pressure to evidence eventual structural change and coalescence of NPs, as eventually observed in other similar systems.[17,18] We performed this study on 7 different crystals, with different core sizes, ligands and structures (see Table 1). Color maps of the diffractograms as function of pressure are plotted for each sample in Fig. 6. The position of the first peak q normalized by its value at ambient pressure is plotted in Fig. 7 for five samples. As expected, we observe a general shift to large q at low pressure. For the low pressure experiment, the compressibility of the supercrystals BCC-2-C12 and FCC-5-C12 are close but the compressibility of the matrix is larger in FCC-5-C12. At larger pressure, we see that the q positions of the peaks starts to decrease for all samples above some pressure P_c, except fo FCC-3-C16. This decrease, incompatible with the distance reduction induced by hydrostatic external pressure, indicates a change in the structure. This critical pressure P_c can be extracted from the plots $q(P)/q_0$ using a polynomial fit around the maximum. The value of P_c are given in Fig. 6, and represented by a black line.

Such transition may be due to non hydrostaticity as methanol–ethanol mixture become less and less hydrostatic above 10 GPa. However, since P_c are not the same for all samples, and even absent for one sample despite the same transmitting medium, this parameter is intrinsic to the samples themselves and thus translates mechanical properties of NPs supercrystals.

In order to check the reversibility of such transition, we performed the measurement while releasing the pressure. The peak position was also fitted and plotted in Fig. 7. As can be seen, all samples except for FCC-3-C16, undergo an irreversible transition. Indeed, the final value of q after coming back from high pressure is reduced by nearly 20%, showing that the sample do not return in its initial state. Interestingly, FCC structures show a good resilience to pressure, with the highest P_c observed: 14 GPa for FCC-7-Ol, 16 GPa for FCC-5-C12 and above 43 GPa for FCC-3-C16. Different parameters can play a role in the mechanical behavior of gold NPs supercrystals under high pressure: the structure, the gold volume fraction, the core diameter, the nature and length of the ligands, the grafting density, the quality of the crystalline order. Unfortunately, the two last parameters can hardly be controlled. Comparing certain samples with each other nevertheless allows us to give precious insights on the effects of some parameters. First, FCC-3-C16 and BCC-3-C12, even if their ligands are different, have and similar gold cores and very close gold volume fractions: 16.7% and 17.8% respectively. Nevertheless the behavior under high pressure is quite different: no structural change for the FCC structure up to 40 GPa and a structural change with the maximum of q observed around 8 Gpa (see Fig. 7c and e). Clearly, the structure seems to play an important role.

The interpretation is similar to the low pressure regime as in FCC, both ligands and void absorb the deformation shifting the critical pressure to higher values. This effect is amplified for

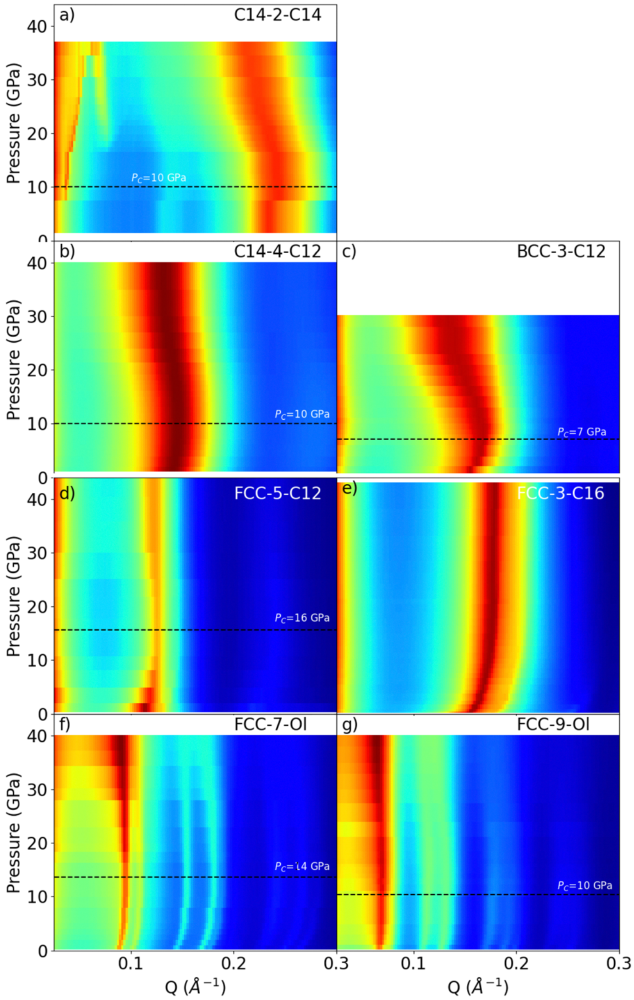

Fig. 6 Color map of the scattering intensity (integrated intensity in log scale) as function of q and pressure for different samples listed in Table 1. The black line correspond to the value of critical pressure P_c related to irreversibility described in the text.

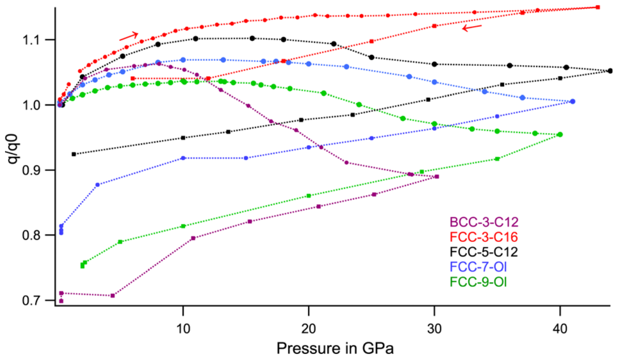

Fig. 7 First peak position $q(P)$, normalized by its value at ambient pressure q_0, for BCC-3-C12 (a = 5.7 nm), FCC-3-16 (a = 7 nm), FCC-5-C12 (a = 9.4 nm), FCC-7-Ol (a = 12.4 nm), FCC-9-Ol (a = 16.5 nm).

sample FCC-3-C16 that remains in FCC structure up to the highest pressure measured of 43 GPa.

In the FCC phase, the transition pressure P_c decreases when the gold volume fraction increases. But FCC-7-Ol and FCC-9-O, having close gold volume fraction, 39.5% and 42,3% respectively, have a significant difference in P_c: 14 and 10 GPa respectively (see Fig. 7f and g) and in the bulk modulus (see Table 3). This confirms that the gold volume fraction is not the only parameter to predict the supercrystal mechanical response. In particular between FCC-7-Ol and FCC-9-Ol, the core structure and its faceting could play a significant role.[40] More generally, for identical supercrystal geometry, the specific properties of the nanoparticles eventually play a role in their mechanical behavior under pressure.

As such irreversible transition can be ascribed to coalescence of the NPs into nanorods or nanowires,[19–21] we performed TEM measurement on the NPs before compresssion and after compression above the critical pressure on FCC-9-Ol (P_c =10 GPa). We thus loaded the DAC with SCs and increased the pressure up to 30 GPa. Once the pressure released, we collected the compressed NPs and performed this multiple times to obtain sufficient mass. The image presented Fig. 8 confirms the presence of coalesced NPs that may be responsible for the irreversibility of the transition.

Other parameters certainly play a role in the mechanical response of the supercrystals but are more difficult to control: the grafting density, the quality of the crystalline order, the exact shape of the core and its faceting. The grafting density as well as the core shape and crystallinity depends on the synthesis procedure. The quality of the crystalline order depends on the NPs polydispersity, on the self-assembly procedure and on the structure. In the FCC structures, large monodomains are mainly observed with textured diffraction patterns whereas in the BCC phase, the crystals are smaller and powder diffraction patterns are commonly measured. In all cases, we observe a broadening of the diffraction peaks upon increasing pressure whereas pressure-induced ordering (annealing effect) of the superstructure was observed in another system.[16] Contrary to our results on gold NPs, the supercrystals built by PbS nanocrystals (6 nm) assembled in the BCC structure have revealed to be more compressible than the allotrope FCC supercrystal.[40] The interpretation was that the nanocrystals in the FCC structure are isotropically oriented, whereas the nanocrystals in the BCC structure exhibit a high degree of orientational ordering. The external shape thus can play an important role when the core size is large enough. The quality of the crystalline order is certainly also a key parameter to understand the supercrystals mechanical response.

Table 3 Mechanical properties of FCC supercrystals: comparison between FCC-5-C12, FCC-7-Ol and FCC-9-Ol:, ϕ_{Gold} is the gold volume fraction in the SC, P_c is the critical pressure in GPa, B^0_{SC} is the measured SC bulk modulus in GPa, and B^0_{Matrix} is the matrix bulk modulus in GPa estimated from B^0_{SC} and the initial gold volume fraction

Name	D_c (nm)	Ligand	ϕ_{Gold}	P_c	B^0_{SC}	B^0_{Matrix}
FCC-5-C12	4.82	C12	26%	16	5.3	4
FCC-7-Ol	7.0	Oleyl.	39%	14	17.5	10.5
FCC-9-Ol	9.6	Oleyl.	41%	10	22.4	13

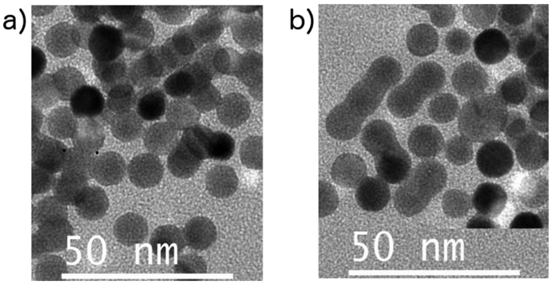

Fig. 8 TEM image of uncompressed FCC-9-Ol NPs (Left) and after compression above 30 GPa (Right). After compression, sintering is observed for some particles instead of just superposition of particles before compression.

4. Conclusions

The extensive high pressure study of several supercrystals of gold NPs detailed here lead us to general conclusions on their mechanical properties. The pressure affects differently the supercrystals depending on their initial structure in a way that hard sphere model is not adequate. In the low pressure regime, the compressibility is governed by the shape of the volume available for each NP, and more precisely its deviation from a sphere. This NP environment dependence explains the strong role of structure in the bulk modulus of supercrystals. From low pressure experiments, we also extract quantitative information with the bulk modulus of the three available structures FCC, BCC and C14 phases. At higher pressure, a quasi-systematic phase transition is observed between 8 and 16 GPa. This transition is irreversible: the structure of the supercrystals obtained after exceeding the critical pressure no longer resembles the initial structure before compression. This irreversibility can be ascribed to sintering of NPS into small rods that cannot be redispersed by releasing the pressure. This interpretation is confirmed by TEM on uncompressed NP and NPs extracted from high pressure cell after exceeding the critical pressure. This extensive study will serve as a reference for future studies of mechanical properties of self assembled superstructures as well as pressure tuning of optical properties of gold supercrystals.

Author contributions

V. B. built the DAC cell and managed all the technical aspects related to the pressure, C. G. synthetized the NPs. B. P. manufactured the gold supercrystals; H. I., V. B. and B. P. performed the measurements, processed the experimental data, performed the analysis, and designed the figures. B. P. drafted the manuscript. All authors discussed the results and commented on the manuscript.

Conflicts of interest

There are no conflicts to declare.

Acknowledgements

We acknowledge SOLEIL for providing the synchrotron radiation facilities and we thank Thomas Bizien for assistance in using beamline SWING (Run 20201484 and Run 20211405). We thank J. F. Sadoc for providing the mathematica drawings of the FCC and BCC Voronoi cells. This work is funded by the French National Research Agency (SoftQC project; **https://softqc.wordpress.com/**; ANR grant ANR-18-CE09-0025).

Notes and references

1 X. Huang and M. A. El-Sayed, *J. Adv. Res.*, 2010, **1**, 13–28.
2 D. García-Lojo, S. Núñez-Sánchez, S. Gómez-Graña, M. Grzelczak, I. Pastoriza-Santos, J. Pérez-Juste and L. M. Liz-Marzán, *Acc. Chem. Res.*, 2019, **52**, 1855–1864.
3 F. Schulz, I. Lokteva, W. J. Parak and F. Lehmkühler, *Part. Part. Syst. Charact.*, 2021, **38**, 2100087.
4 B. Pansu, C. Goldmann, D. Constantin, M. Impéror-Clerc and J.-F. Sadoc, *Soft Matter*, 2021, 6461.
5 K. Bian, H. Schunk, D. Ye, A. Hwang, T. S. Luk, R. Li, Z. Wang and H. Fan, *Nat. Commun.*, 2018, **9**, 2365.
6 T. K. Patra, H. Chan, P. Podsiadlo, E. V. Shevchenko, S. K. R. S. Sankaranarayanan and B. Narayanan, *Nanoscale*, 2019, **11**, 10655–10666.
7 T. Kister, D. Monego, P. Mulvaney, A. Widmer-Cooper and T. Kraus, *ACS Nano*, 2018, **12**, 5969–5977.
8 B. Pansu and J. F. Sadoc, *Eur. Phys. J. E*, 2017, **40**, 102.
9 K. J. Si, Y. Chen, Q. Shi and W. Cheng, *Adv. Sci.*, 2018, **5**, 1700179.
10 M. Gauvin, Y. Wan, I. Arfaoui and M.-P. Pileni, *J. Phys. Chem. C*, 2014, **118**, 5005–5012.
11 M.-P. Pileni, *EPL*, 2017, **119**, 37002.
12 A. Çolak, J. Wei, I. Arfaoui and M.-P. Pileni, *Phys. Chem. Chem. Phys.*, 2017, **19**, 23887–23897.
13 D. Giuntini, A. Davydok, M. Blankenburg, B. Domènech, B. Bor, M. Li, I. Scheider, C. Krywka, M. Müller and G. A. Schneider, *Nano Lett.*, 2021, **21**, 2891–2897.
14 C. Yan, B. Bor, B. Domènech, G. A. Schneider and D. Giuntini, *JOM*, 2022, **74**, 2261–2276.
15 K. Pilar, V. Balédent, M. Zeghal, P. Judeinstein, S. Jeong, S. Passerini and S. Greenbaum, *J. Chem. Phys.*, 2018, **148**, 30–33.
16 P. Podsiadlo, B. Lee, V. B. Prakapenka, G. V. Krylova, R. D. Schaller, A. Demortière and E. V. Shevchenko, *Nano Lett.*, 2011, **11**, 579–588.
17 H. Wu, F. Bai, Z. Sun, R. E. Haddad, D. M. Boye, Z. Wang and H. Fan, *Angew. Chem., Int. Ed.*, 2010, **49**, 8431–8434.
18 H. Wu, F. Bai, Z. Sun, R. E. Haddad, D. M. Boye, Z. Wang, J. Y. Huang and H. Fan, *J. Am. Chem. Soc.*, 2010, **132**, 12826–12828.
19 B. Li, X. Wen, R. Li, Z. Wang, P. G. Clem and H. Fan, *Nat. Commun.*, 2014, **5**, 4179.
20 J. Zhu, Z. Quan, C. Wang, X. Wen, Y. Jiang, J. Fang, Z. Wang, Y. Zhao and H. Xu, *Nanoscale*, 2016, **8**, 5214–5218.

21 B. Li, K. Bian, X. Zhou, P. Lu, S. Liu, I. Brener, M. Sinclair, T. Luk, H. Schunk, L. Alarid, P. G. Clem, Z. Wang and H. Fan, *Sci. Adv.*, 2017, **3**, e1602916.

22 H. Ibrahim, V. Balédent, M. Impéror-Clerc and B. Pansu, *RSC Adv.*, 2022, **12**, 23675–23679.

23 M. Brust, M. Walker, D. Bethell, D. J. Schiffrin and R. Whyman, *J. Chem. Soc., Chem. Commun.*, 1994, 801–802.

24 C. Goldmann, C. Moretti, B. Mahler, B. Abécassis, M. Impéror-Clerc and B. Pansu, *Chem. Commun.*, 2021, **57**, 12512–12515.

25 Y. Zheng, X. Zhong, Z. Li and Y. Xia, *Part. Part. Syst. Charact.*, 2014, **31**, 266–273.

26 F. Schulz, S. Tober and H. Lange, *Langmuir*, 2017, **33**, 14437–14444.

27 H. Hinterwirth, S. Kappel, T. Waitz, T. Prohaska, W. Lindner and M. Lämmerhofer, *ACS Nano*, 2013, **7**, 1129–1136.

28 X. Ye, C. Zhu, P. Ercius, S. N. Raja, B. He, M. R. Jones, M. R. Hauwiller, Y. Liu, T. Xu and A. P. Alivisatos, *Nat. Commun.*, 2015, **6**, 10052.

29 T. Cosgrove, S. Swier, R. Schmidt, S. Muangpil, Y. Espidel, P. Griffiths and S. W. Prescott, *Langmuir*, 2015, **31**, 8469–8477.

30 A. D. Chijioke, W. J. Nellis, A. Soldatov and I. F. Silvera, *J. Appl. Phys.*, 2005, **98**, 114905.

31 A. Dewaele, P. Loubeyre and M. Mezouar, *Phys. Rev. B: Condens. Matter Mater. Phys.*, 2004, **70**, 094112.

32 C. Martín-Sánchez, A. Sánchez-Iglesias, J. A. Barreda-Argüeso, A. Polian, J.-P. Itié, J. Pérez, P. Mulvaney, L. M. Liz-Marzán and F. Rodríguez, *ACS Nano*, 2021, **15**, 19128–19137.

33 J. Rault, *Eur. Phys. J. E: Soft Matter Biol. Phys.*, 2014, **37**, 113.

34 K. Kim, M. W. Schulze, A. Arora, R. M. Lewis, M. A. Hillmyer, K. D. Dorfman and F. S. Bates, *Science*, 2017, **356**, 520–523.

35 P. Schwerdtfeger and A. Burrows, *J. Phys. Chem. C*, 2022, **126**, 8874–8882.

36 D. V. Leff, P. C. Ohara, J. R. Heath and W. M. Gelbart, *J. Phys. Chem.*, 1995, **99**, 7036–7041.

37 A. Phua, J. Smith, C. H. J. Davies, P. S. Cook and G. W. Delaney, *Powder Technol.*, 2023, **418**, 118272.

38 K. D. Dorfman, *Macromolecules*, 2021, **54**, 10251–10270.

39 S. Lee, C. Leighton and F. S. Bates, *Proc. Natl. Acad. Sci. U. S. A.*, 2014, **111**, 17723–17731.

40 K. Bian, Z. Wang and T. Hanrath, *J. Am. Chem. Soc.*, 2012, **134**, 10787–10790.